Biomaterials Science

PAPER

View Article Online
View Journal

Cite this: DOI: 10.1039/d6bm00291a

Design and validation of a bioactive and antimicrobial coating through advanced deposition strategies for biomedical applications

Giusy Sorvillo,[a,b] Rosa Calderon-Jacinto,[a] Yijie Li,[b] Léa Magne,[b] Cynthia Calligaro,[b] Rémy Agniel,[a] Grégory Francius,[d] Nicolas Courtois,[c] Philippe Lavalle,[b,d] Damien Seyer,[a] Nihal Engin Vrana,[b] Emmanuel Pauthe*[a] and Adeline Gand*[a]

peri-Implant infections remain a major challenge to the long-term biointegration of dental implants, requiring coating strategies that simultaneously prevent bacterial infection and promote soft tissue integration. Here, we report a bifunctional polyelectrolyte multilayer Layer-by-Layer (LbL) coating combining poly(L-lysine) (PLL_{30}), hyaluronic acid (HA), and fibronectin (Fn) rationally engineered through architectural control and translated from dip-coating to a clinically applicable spray-assisted deposition. Multilayers were fabricated by dip-coating, with Fn either intercalated throughout the film or confined to the outermost layers. Systematic optimization established that terminal confinement of Fn – Top-Layer Fn architecture $(PLL_{30}\text{-}HA)_6 + (PLL_{30}\text{-}Fn)_6$ – achieves complete inhibition of bacterial adhesion against *Staphylococcus aureus* and *Aggregatibacter actinomycetemcomitans* while maintaining cytocompatibility (78% human gingival fibroblast viability), whereas intercalating Fn throughout the film compromises cell compatibility, despite equivalent inhibition of bacterial adhesion. This architecture was successfully translated to a clinically scalable spray-assisted deposition using a dual-syringe spray device (coating time < 1 minute). Spray-coated titanium preserved bifunctionality achieving a significant reduction of *S. aureus* and a complete inhibition of *A. actinomycetemcomitans*, and 88% fibroblast viability after serum coating preconditioning. This work establishes a translational pathway of bifunctional coatings to clinical application, offering possibilities for both preventive and curative strategies against *peri*-implantitis and other implant-associated infections.

Received 27th February 2026,
Accepted 1st June 2026

DOI: 10.1039/d6bm00291a

rsc.li/biomaterials-science

Introduction

Dental implants have emerged as a standard treatment for tooth replacement, with prevalence among adults with missing teeth in the United States increasing substantially over the past two decades, and continuing to rise driven by an ageing population and improved clinical outcomes.[1,2] Despite exhibiting high survival rates exceeding 95% over a decade, *peri*-implantitis remains a major biological complication that jeopardizes the long-term success of implants.[3,4] *peri*-implantitis is characterized by progressive bone resorption around osseointegrated implants, primarily driven by the accumulation of bacterial biofilm at the implant–soft tissue interface.[5] Systematic reviews report a patient-level prevalence ranging from 10% to 45%, with substantial variability depending on diagnostic criteria and follow-up duration.[6,7] Current therapeutic approaches, including mechanical debridement, systemic antibiotics, and surgical interventions, often fail to prevent disease recurrence and do not ensure long-term stability.[8] The increasing use of dental implants, combined with the limited efficacy of existing treatments, highlights the urgent need for preventive and curative strategies that address the root causes of *peri*-implantitis. The pathogenesis of *peri*-implantitis is fundamentally linked to two interrelated factors: bacterial colonization and inadequate soft tissue sealing around the implant. Unlike natural teeth, which benefit from a robust periodontal attachment including cementum, periodontal ligament, and junctional epithelium, dental implants rely on a weaker *peri*-implant seal formed primarily by hemidesmosomal attachments to the titanium surface.[9] This compromised barrier facilitates bacterial penetration into the *peri*-implant sulcus, where biofilm formation initiates an inflammatory cascade leading to connective tissue breakdown and bone resorption.

[a]*ERRMECe Laboratory, Biomaterials for Health Group, CY Cergy Paris University, 1 rue Descartes, 95000 Neuville sur Oise, France. E-mail: emmanuel.pauthe@cyu.fr, adeline.gand@cyu.fr*
[b]*SPARTHA Medical, Strasbourg Center for Biomedical Research (CRBS), 1 rue Eugène Boeckel, Strasbourg, France*
[c]*Anthogyr SAS, 2237 Avenue A. Lasquin, 74700 Sallanches, France*
[d]*Inserm UMR_S 1121, CNRS EMR 7003, University of Strasbourg, Biomaterials and Bioengineering, Strasbourg Center for Biomedical Research (CRBS), 1 rue Eugène Boeckel, Strasbourg, France*

The clinical outcome is ultimately determined by the "race to the surface" between host cells and bacteria.[10] If fibroblasts and epithelial cells colonize the implant surface first and establish a stable biological seal, bacterial adhesion is impeded. Conversely, if bacteria prevail in this competition, biofilm formation becomes irreversible and highly resistant to both host immune responses and antimicrobial treatments.[11] The microbial etiology of *peri*-implantitis involves complex polymicrobial biofilms. It starts with *Actinomyces* and *Streptococci* species acting as early colonizers, which modify the local environment to facilitate subsequent attachment of late colonizers.[12,13] *Aggregatibacter actinomycetemcomitans*, a Gram-negative periodontal pathogen, is particularly associated with aggressive forms of *peri*-implantitis and detected in high prevalence around failing implants.[14,15] Another pathogen usually associated with implant infection is *Staphylococcus aureus*, a Gram-positive bacteria implicated in early implant failure due to its strong ability to adhere to titanium surfaces and form robust biofilms.[16–18] Therefore, an effective strategy must tip the balance between soft tissue integration and broad-spectrum antibacterial activity against both Gram-positive and Gram-negative bacteria.

Various surface modification strategies have been developed to address these challenges, but most focus on either antibacterial properties or tissue integration in isolation. Antibacterial approaches include coatings loaded with antibiotics, silver nanoparticles, or antimicrobial peptides, as well as intrinsically antibacterial polymers such as chitosan.[19,20] While effective against bacteria, these strategies often lack pro-adhesive properties for host cells. Conversely, strategies aimed at enhancing soft tissue integration have focused on surface topography modifications, increased hydrophilicity, and grafting of extracellular matrix proteins such as fibronectin or adhesion peptides like RGD.[21–23] Although these approaches improve fibroblasts and keratinocytes adhesion, they typically do not provide antibacterial protection, leaving the implant vulnerable to infection. The lack of multifunctional strategies that simultaneously promote tissue integration and prevent bacterial colonization represents a significant gap in current implant surface engineering. Addressing this gap requires both rational architectural design – integrating antibacterial and pro-adhesive functionalities within a single coating – and advanced deposition strategies capable of translating laboratory-validated architectures into clinical application processes.

In this context, interfaces generated by the Layer-by-Layer (LbL) assembly technique appear particularly relevant, as they provide a versatile platform for designing multifunctional implant coatings capable of addressing this dual challenge. Based on the sequential adsorption of oppositely charged polyelectrolytes, LbL assembly enables the construction of nanoscale films with precisely controlled composition, thickness, and architecture.[24] Unlike covalent grafting methods, LbL can be applied to virtually any substrate geometry without harsh chemical treatments, making it particularly suitable for complex implant surfaces. Moreover, LbL films can serve as reservoirs for bioactive molecules, allowing tunable release kinetics and sustained biological activity.[25–27]

A major advantage of the LbL approach is its compatibility with various deposition techniques, including dip coating, spin coating, and spray coating.[28] Notably, the core principles are preserved regardless of the deposition method. In this study we investigated two strategies: (i) conventional dip-coating, which allows precise control over film architecture for systematic optimization; (ii) spray-assisted deposition, which enables rapid fabrication of coatings on complex 3D geometries, supporting *in situ* application on implanted devices for both preventive and curative clinical treatment.

Previous research has highlighted the potential of individual LbL components for either antibacterial or pro-adhesive functions. Specifically, short-chain poly(L-arginine hydrochloride) with 30 arginine residues (PAR_{30}) combined with hyaluronic acid (HA) has demonstrated strong antibacterial activity. This effect is associated with an exponential growth regime that promotes high polycation diffusivity, which underlies the bacterial contact-killing properties of the film through membrane-disruption mechanisms.[29] Conversely, poly(L-lysine) with 30 residues (PLL_{30}), combined with fibronectin (Fn), a key component of the extracellular matrix, enhance fibroblast adhesion and proliferation while reducing early bacterial attachment.[30] However, the integration of these components into a single bifunctional coating, and the optimization of multilayer architecture to maximize both functions simultaneously, remains unexplored.

This study examines two central hypotheses: (i) that the spatial positioning of Fn within PLL_{30}/HA multilayers significantly influences fibroblast adhesion without compromising the inherent antibacterial activity of the polycation, and (ii) that the optimized architecture can be successfully translated from dip-coating to a rapid spray-deposition system suitable for chairside clinical application.

To address the first hypothesis, we systematically compared two architectural configurations fabricated by dip-coating on glass substrates to identify the optimal strategy for maximizing Fn surface accessibility for cell adhesion while maintaining antibacterial efficacy: (i) intercalated Fn architecture $[(PLL_{30}\text{-}HA)_2(PLL_{30}\text{-}Fn)]_4$, where Fn alternates with HA throughout the film thickness, and (ii) Top-Layer Fn architecture $(PLL_{30}\text{-}HA)_6 + (PLL_{30}\text{-}Fn)_6$, where Fn is confined to the terminal surface layers deposited onto a pre-assembled $(PLL_{30}\text{-}HA)_6$ base. PLL_{30} was selected over the polycation PAR_{30} due to its previously validated successful combination with Fn,[30] ensuring biocompatibility at the critical implant–gingiva interface.

To evaluate the second hypothesis, the optimized architecture identified through dip-coating studies was adapted to an innovative dual-syringe spray coating system developed by SPARTHA Medical, and validated on medical-grade titanium alloy (Ti6Al4V-ELI).

This study demonstrates for the first time the feasibility of designing a single LbL coating architecture that simultaneously provides antibacterial protection and maintains a surface conducive to gingival fibroblast attachment by strategically combining PLL_{30}, HA and Fn in a stratified multilayer structure (Scheme 1A).

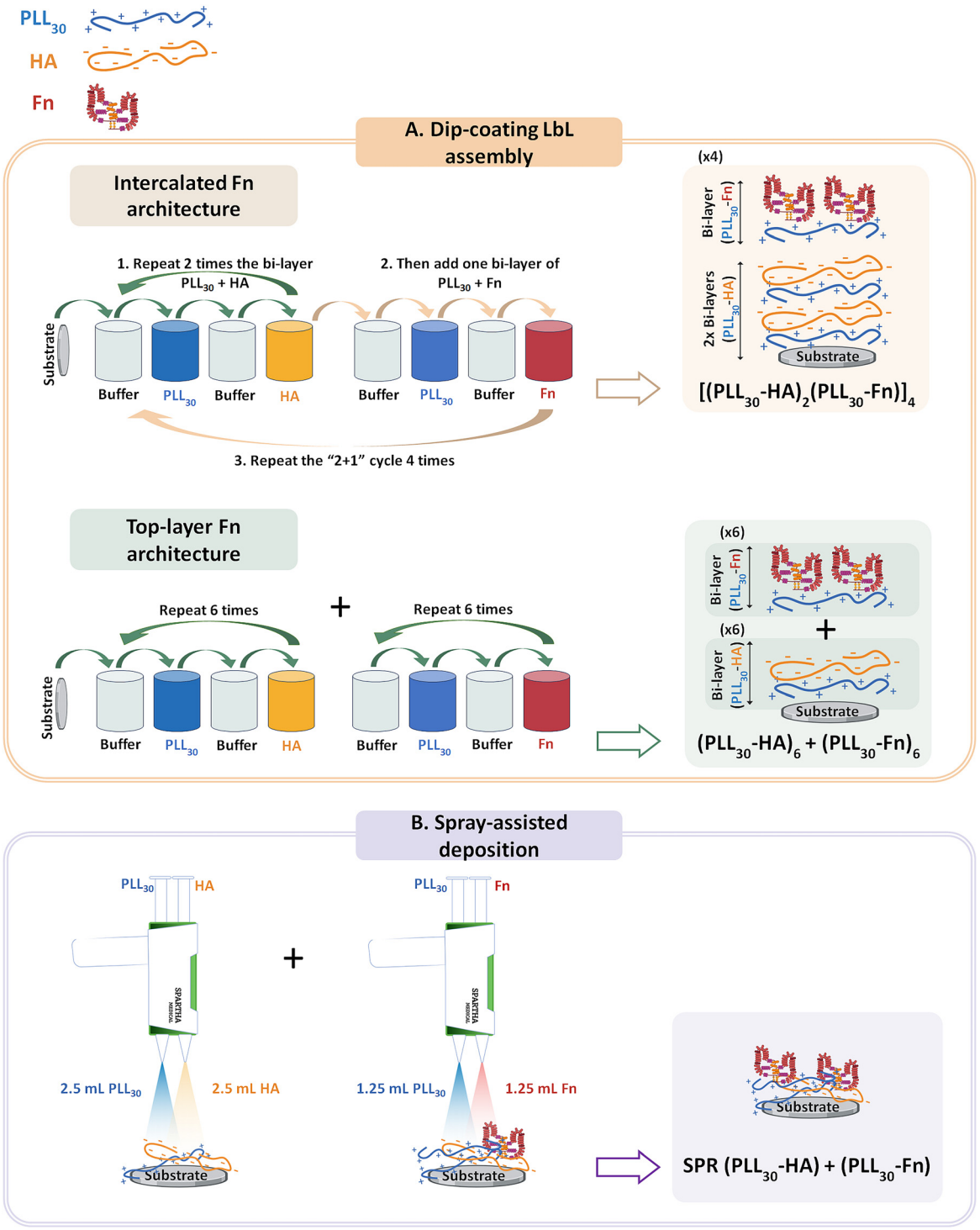

Scheme 1 Schematic illustration of dip-coating and spray-coating assembly. (A) Dip-coating LbL assembly of the two coating designs. In the Intercalated Fn architecture, two consecutive bilayers of PLL_{30}-HA followed by one bilayer of PLL_{30}-Fn were deposited, and the "2 + 1" sequence was repeated four times, yielding a total of 12 bilayers. In the Top-Layer Fn architecture, six PLL_{30}-HA bilayers were first assembled, followed by six PLL_{30}-Fn bilayers. (B) Spray-assisted deposition using the dual-syringe spray system (SPARTHA Medical), for the simultaneous deposition of PLL_{30} (polycation, blue) with HA (polyanion, orange) or Fn (polyanion, red). Solutions were sprayed vertically onto horizontally positioned substrates, using 2.5 mL of PLL_{30} and HA and 1.25 mL of the PLL_{30} and Fn. The architecture consists of a sprayed PLL_{30}-HA base followed by PLL_{30}-Fn sprayed on top.

Moreover, this architecture was successfully translated to an advanced spray-assisted deposition onto clinically relevant titanium surfaces (Scheme 1B).

Experimental

Materials and methods

Coating materials. Human plasmatic fibronectin (Fn) was purified from human plasma using a three-step affinity chromatography process.[31] Protein concentration was determined by UV absorbance at 280 nm using an extinction coefficient $A_1\%$ = 12.8. Purity was assessed to be approximately 98% (w/w) by SDS-PAGE analysis.

Sodium hyaluronate (HA, molecular weight 100–180 kDa) was purchased from Lifecore Biomedical (Chaska, MN, USA) and HTL Biotechnology (France). Poly-L-lysine hydrobromide ($PLLKB_{30}$, MW 6300 Da, 30 residues) and poly-L-lysine hydrochloride ($PLLKC_{30}$, MW 4900 Da, 30 residues) were purchased from Alamanda Polymers (Huntsville, AL, USA). All dip-coating experiments employed $PLLKB_{30}$, while spray-coating experiments employed $PLLKC_{30}$.

All solutions were prepared in sterile-filtered (0.22 μm) Tris-NaCl buffer (10 mM Tris, 150 mM NaCl, pH 7.4).

Substrates. Round borosilicate glass coverslips (12 mm diameter, 0.17 mm thickness) were obtained from Thermo Fisher Scientific (New York, NY, USA). Medical-grade titanium alloy discs (Ti6Al4V-ELI, 9 mm diameter, 1 mm thickness, ISO 5832-3 compliant) with machined surface finish (Ra < 0.2 μm) were provided by Anthogyr SAS (Sallanches, France).

Layer-by-Layer (LbL) assembly methods

Dip-coating assembly. Two architectural configurations were evaluated (Scheme 1A): (i) Top-Layer Fn architecture, $(PLL_{30}\text{-}HA)_6 + (PLL_{30}\text{-}Fn)_6$, substrates were first coated of a base of six PLL_{30}-HA bilayers, followed by six PLL_{30}-Fn bilayers as terminal layers. This configuration confines Fn to the outermost surface. (ii) Intercalated Fn architecture, $[(PLL_{30}\text{-}HA)_2(PLL_{30}\text{-}Fn)]_4$, substrates were coated with alternating blocks of two PLL_{30}-HA bilayers and one PLL_{30}-Fn bilayer, the "2 + 1" cycle was repeated four times. This configuration distributes Fn throughout the film thickness.

Films are constructed with HA and Fn as polyanions and PLL_{30} as polycation on 12 mm-diameter glass slides or on silicon crystals, pretreated with piranha solution (20% H_2O_2, 20% H_2SO_4). All solutions were prepared at 0.5 mg mL^{-1} in Tris-NaCl buffer. Substrates were dipped alternately in the polycation and polyanion solutions with different exposure time: 5 min for PLL_{30} and HA, 15 min for the first three layers of Fn and 8 min for the remaining layers.[30,32] Each deposition is followed by three 1 min buffer rinse steps. Following assembly, samples were let air-dried and stored at room temperature.

Spray-coating assembly. Spray-coating was performed using the dual-syringe spray device developed and patented by SPARTHA Medical SAS (Strasbourg, France). This system enables simultaneous nebulization of polycation and polyanion solutions from independent reservoirs, eliminating the need for intermediate rinsing steps and reducing total coating time to less than one minute.

PLL_{30}: 10 mg mL^{-1}, HA: 5 mg mL^{-1} and Fn: 1.0 mg mL^{-1} were prepared in Tris-NaCl buffer. Substrates were mounted on custom 3D-printed carriers designed using SolidWorks software (Dassault Systèmes, Vélizy-Villacoublay, France) and manufactured with an Ultimaker S3 FDM printer (UltiMaker, Utrecht, Netherlands). Coating deposition involves perpendicular spray of solutions on a horizontally oriented substrate at 10 cm distance between the spray nozzle and the substrate, moving the spray device in a continuous horizontally linear motion (left-to-right and return) ensuring uniform coverage. Eight samples were coated simultaneously. Coated samples were air-dried horizontally and stored at room temperature before biological testing. Coating deposition proceeded in two sequential steps without intermediate rinsing or drying steps: 2.5 mL of $PLLKC_{30}$/HA were sprayed on the substrates to construct the (PLL_{30}-HA) base layers followed by 1.25 mL of $PLLKC_{30}$/Fn to construct the (PLL_{30}-Fn) terminal layers (Scheme 1B).

Physicochemical characterization

Attenuated total reflection-Fourier transform infrared spectroscopy (ATR-FTIR). ATR-FTIR spectra were recorded using a Tensor 27 spectrophotometer (Bruker, Mannheim, Germany) equipped with an MCT detector. A horizontal ATR accessory (HATR, PIKE Technologies, Fitchburg, WI, USA) with a 45° trapezoidal silicon internal reflection element (IRE, 80 × 10 × 2 mm) was employed. Solutions were prepared at 0.5 mg mL^{-1} in a deuterated Tris-NaCl buffer. Each solution was exposed to the silicon crystal for the designated adsorption time (5 to 15 min), followed by three buffer rinses (1 min each). Spectra were acquired as an average of 64 scans over the range 800–4000 cm^{-1} with 4 cm^{-1} resolution using Blackman–Harris three-term apodization. Film growth was quantified by integrating the amide I′ band (1600–1700 cm^{-1}) using OPUS software version 7.2 (Bruker, Mannheim, Germany).

Quartz crystal microbalance with dissipation (QCM-D). Real-time mass deposition and viscoelastic properties were monitored using a Q-Sense E1 system (Biolin Scientific, Gothenburg, Sweden) equipped with silicon coated quartz crystals. Prior to use, crystals were cleaned by 2% (w/v) Hellmanex solution (45 min) and HCl 1M solution (15 min) and rinsed with ultrapure water. Polyelectrolyte and protein solutions (0.5 mg mL^{-1} in Tris-NaCl buffer) were introduced sequentially at a flow rate of 400 μL min^{-1} with intermediate 5 min buffer rinse. The deposition time was: 5 min for PLL_{30} and HA and until crystal stability for Fn. Changes in resonance frequency ($-\Delta f\nu$) and energy dissipation (ΔD) were recorded. Data from the $-\Delta f3$ are presented.

Confocal laser scanning microscopy (CLSM). Spray-assisted multilayer assembly on Ti6Al4V-ELI substrates was assessed by confocal laser scanning microscope (LSM 900 Carl Zeiss,

Germany) using fluorescently labeled components. Images were acquired with a 20× objective using sequential scanning mode to minimize crosstalk between channels, and *Z*-stacks were collected. All images were processed using ImageJ software (NIH, USA).

PLL_{30} was labeled with fluorescein isothiocyanate (FITC, Sigma-Aldrich, Saint-Quentin-Fallavier, France) following adaptation of established protocol.[29] Briefly, PLL_{30} (1 mg mL^{-1}) in freshly prepared sodium bicarbonate buffer (100 mM $NaHCO_3$, pH 8.3) was mixed with FITC at a 1 : 2 molar ratio (PLL_{30} : FITC), under light protection with magnetic stirring at room temperature for 16 h. Unreacted dye was removed by dialysis (MWCO 3500 Da) against Tris-NaCl buffer (4 L exchanges every 6 h, four total exchanges over 48 h).

Fn was labeled with Alexa Fluor 568 carboxylic acid, succinimidyl ester (Thermo Fisher Scientific, New York, NY, USA). Fn (4 mg) was dialyzed against sodium carbonate–bicarbonate buffer (0.1 M, pH 8.3) at 4 °C (2 h + overnight) using 12–14 kDa MWCO tubing. Fn concentration was adjusted to 2 mg mL^{-1}, and Alexa Fluor 568 dye was added at a ratio of 5 µL dye solution per 1 mL Fn solution. After 1 h incubation at room temperature with gentle agitation in the dark, excess dye was removed by size-exclusion chromatography (Sephadex G-25 gel column, Sigma-Aldrich, Saint-Quentin-Fallavier, France). Labeled Fn (Fn*) concentration was determined spectrophotometrically: $A_{prot} = A_{280} - (A_{568} \times 0.46)$, and $[Fn^*] = A_{prot}/1.28$. Fn* was filter-sterilized, aliquoted, and stored at 4 °C protected from light.

Fn* was incorporated directly during spray coating at 1 : 100 (v/v) ratio with unlabeled Fn. PLL_{30}-FITC was introduced by brief incubation (15 min) of pre-fabricated spray-coated as previously reported for PLL_{30}-based films.[33,34]

Atomic force microscopy. Atomic force microscopy (Nanowizard 4, Bruker) was used to image the thickness and the topography of the dip-coated and spray-coated films on glass substrates, rehydrated for at least 2 h in PBS 0.1 M pH 7.4, using the PEAKFORCE-HIRS-SSB PeakForce Tapping™ AFM Probes. Images and surface roughness were analysed using Gwyddion software (Gwyddion.net). To account for the heterogeneous nature of the coating surfaces, the mean roughness values (Sa) were extracted independently from small regions of interest corresponding to three distinct surface features: (i) bare glass areas exposed by scratch, (ii) lower coating regions; and (iii) aggregate features.

Enzyme-linked immunosorbent assay (ELISA). The accessibility of Fn and its cell-binding domain (CBD) within the Intercalated Fn architecture, Top-Layer Fn architecture and Fn monolayer as control reference was tested using ELISA with specific antibodies. Coated glass discs (12 mm diameter) placed in 24-well plates were blocked for 1 h at room temperature with PBS containing 3% (w/v) milk powder (blocking buffer). 2 h incubation at room temperature with primary antibody against the Fn (F3648 Anti-Fibronectin antibody produced in rabbit, Sigma) or Fn cell-binding domain (sc18825 mouse IgG Santa Cruz) at 1/1000 diluted in PBS + 0.05% Tween® 20 + 1% milk powder was then performed. Then samples were washed three times with PBS-Tween® 0.05% (PBST). The secondary antibody anti rabbit IgG-peroxidase (NA934, Cytiva) or anti mouse IgG-peroxidase (NA931, Cytiva) 1/5000 diluted in PBS + 0.05% Tween® + 1% milk powder was incubated for 1 h at room temperature. Three washes with PBST followed by two washes with PBS were done and remaining antibodies were revealed with a 3.3′.5.5′-tetramethylbenzidine (TMB) substrate from 5 to 30 min. The reaction was stopped by sulfuric acid 1 M and absorbance was measured at 450 nm using a microplate reader.

Cytocompatibility evaluation

Cell lines and culture media. Primary human gingival fibroblasts (HGF) were isolated from healthy gingival tissue and kindly donated by UMR1333 Oral Health (Université Paris Cité, France). Cells were maintained in Dulbecco's Modified Eagle's medium (DMEM) with high glucose (4.5 g L^{-1}, Gibco) supplemented with 10% (v/v) heat-inactivated fetal bovine serum (FBS, Gibco), 1% (v/v) penicillin–streptomycin (100 U mL^{-1} and 100 µg mL^{-1}, respectively, Gibco), and 1% (w/v) sodium bicarbonate. Cells at passages < 10 were used for experiments. Murine Balb/3T3 clone A31 fibroblasts (ATCC CCL-163, ATCC, Manassas, VA, USA) were cultured in DMEM with high glucose supplemented with 10% FBS and 1% penicillin–streptomycin and work under 70–80% of confluency. All cells were maintained at 37 °C at 5% CO_2.

Cell metabolic activity assay (HGF, 24 h) on dip coatings. Dip-coated and uncoated sterile glass substrates were placed in 24-well plates. HGF cells were seeded at a density of 20 000 cells per cm^2 in complete DMEM and incubated for 24 h at 37 °C, 5% CO_2. Cell metabolic activity was assessed using the resazurin reduction assay (alamarBlue™, Sigma-Aldrich, Saint-Quentin-Fallavier, France). Briefly, culture medium was replaced with fresh complete medium containing 10% (v/v) resazurin reagent, and cells were incubated for an additional 3 h. After incubation, 150 µL of the medium of each well was transferred to a black 96-well plate. Fluorescence intensity was measured using a microplate reader (excitation 560 nm, emission 590 nm). Results are expressed as relative fluorescence units normalized to uncoated control substrates. Materials exhibiting ≥ 70% cell viability relative to controls are considered non-cytotoxic (ISO 10993-5).

Early cell adhesion assay (Balb/3T3, 4 h) and metabolic activity assay (Balb/3T3, 24 h) on spray coatings. To evaluate initial cell attachment, Balb/3T3 cells were seeded onto sterile pre-coated or uncoated sprayed glass substrates using a droplet at a density of 300 000 cells per sample, in complete DMEM and allowed to adhere for 15 min at 37 °C, 5% CO_2. Subsequently, complete medium containing 10% (v/v) resazurin reagent was gently added to each well, and cells were incubated for an additional 4 h. To evaluate cell adhesion and spreading, Balb/3T3 cells were seeded onto sterile pre-coated or uncoated sprayed titanium substrates at a density of 40 000 cells per sample and incubate them for 24 h at 37 °C with 5% CO_2. Two conditions were tested to assess the effect of serum protein pre-conditioning: (i) direct seeding: cells seeded

directly onto spray-coated surfaces without pre-treatment, (ii) FBS pre-conditioning: substrates pre-incubated with FBS (1 h, 37 °C, 5% CO_2) before cell seeding to simulate physiological serum protein adsorption. After 24 h, culture medium was replaced with fresh DMEM containing 10% (v/v) resazurin reagent (alamarBlue™, Sigma-Aldrich) and cells were incubated for 3 h at 37 °C with 5% CO_2. Metabolic activity was quantified by fluorescence measurement as described above.

HGF morphology on dip-coated glass substrates. A total of 20 000 cells per cm^2 were seeded on sterile substrates using complete medium and incubated at 37 °C and 5% CO_2 during 24 h. Cells were fixed with a 4% (w/v) *para*-formaldehyde solution (AlfaAesar, Haverhill, MA, USA) diluted in PBS for 15 min at room temperature and permeabilized with 0.2% (v/v) Triton X-100 (Sigma-Aldrich, Saint-Quentin-Fallavier, France) for 15 min. Non-specific binding sites were blocked with a 0.2% (w/v) bovine serum albumin (BSA) solution in PBS containing 0.1% Tween® 20 (Sigma-Aldrich, Saint-Quentin-Fallavier, France) (PBT) for at least 15 min. Samples were incubated with mouse monoclonal anti-vinculin (V9131; Sigma-Aldrich, Saint-Quentin-Fallavier, France) diluted 1 : 400 in PBT for 45 min at room temperature. After 3 washes in PBS, samples were incubated in a humidity chamber for 1 h with a mixture of Alexa Fluor™ 488 goat anti-mouse IgG secondary antibody (A11029; Invitrogen, Eugene, OR, USA) diluted 1 : 1000, with Alexa Fluor 568 phalloidin (A12380; Invitrogen, Eugene, OR, USA) diluted 1 : 400 and 4′,6-diamidino-2-phenylindole dihydrochloride (DAPI; Sigma-Aldrich, Saint-Quentin-Fallavier, France) at 0.5 μg ml^{-1}, all diluted in PBT, thereby enabling simultaneous visualisation of focal adhesions, actin filaments of cytoskeleton and nuclei. Finally, samples were washed 3 times with PBS, mounted in ProLong™ Gold (Invitrogen, Eugene, OR, USA), and examined with a LSM 900 confocal laser scanning microscope (Carl Zeiss, Iena, Germany) using a 40× objective and sequential scanning mode. *Z*-Stacks were converted to 2D images with ImageJ software (NHI, USA).

Antibacterial assays

Bacterial strains and culture conditions. *Staphylococcus aureus* ATCC 25923 was obtained from ATCC (Manassas, VA, USA). *Staphylococcus aureus* CIP 4.83 and *Aggregatibacter actinomycetemcomitans* DSM 8324 were obtained from the "Collection de l'Institut Pasteur" (Paris, France) and from the DSMZ-German collection (Leibniz Institute, Brunswick, Germany), respectively. Bacterial stocks were maintained at −20 °C in culture medium supplemented with 30% (v/v) glycerol. For experiments, bacteria were cultured into Tryptic Soy Broth (TSB) or Mueller Hinton Broth (MHB) and grown overnight (16–18 h) at 37 °C with orbital shaking (200 rpm). Bacterial suspensions were quantified by measuring optical density at 600 nm (OD_{600}). Suspensions were diluted in sterile growth medium or PBS to achieve the desired inoculum density.

Early bacterial adhesion assay (2 h). Dip-coated and uncoated sterile substrates were placed in sterile 24-well tissue culture plates. Bacterial suspensions (10^6 CFU mL^{-1} in PBS) were added to each well and incubated at 37 °C for 2 h under static conditions. Non-adherent bacteria were removed by gently aspirating the supernatant and washing twice with sterile PBS solution. Adherent bacteria were detached by placing samples in a new well plate covered in 0.5 mL 0.9% (w/v) NaCl solution and sonicating in a water bath for 10 min, repeated twice with fresh saline. The combined suspensions were serially diluted (1 : 10), and 100 μL aliquots from appropriate dilutions were spread onto TSA plates. After incubation at 37 °C for 24 h, colony-forming units (CFUs) were counted from plates containing 30–300 colonies. Results are expressed as CFU cm^{-2} of substrate surface area.

Biofilm formation assay (8 h and 24 h) on dip-coated substrates. To assess the bacterial biofilm formation, the same procedure as above followed, except that before sonication the bacteria after 2 h were rinsed and changed wellplate, then added diluted medium (10% TSB in PBS) and let them grow for another 6 or 22 h at 37 °C under static conditions. Quantification was performed by CFUs counting as described above.

Biofilm formation assay (24 h) on spray-coated substrates. To assess the effect of spray coatings on bacterial growth in the surrounding medium, substrates were incubated with bacterial suspensions (10^5 CFU cm^{-2} in MHB or TSB) for 24 h at 37 °C under continuous stirring. Following incubation, the supernatant from each well was transferred to a 96-well microplate, and planktonic bacterial growth was quantified by measuring absorbance at 600 nm. Results are reported as normalized OD_{600} values, with uncoated substrates serving as positive controls for unrestricted bacterial growth. To quantify the adhered bacteria, the same procedure as described above was followed.

Statistical analysis. All experiments were performed with at least three technical replicates. Data are presented as mean ± standard deviation (SD). Statistical significance was assessed using one-way ANOVA using GraphPad Prism version 9.0 (GraphPad Software, San Diego, CA, USA). A p-value < 0.05 was considered statistically significant.

Results and discussion

Design and characterization of dip-coated multilayers

To engineer multifunctional surface coatings that simultaneously combine antibacterial activity and pro-adhesive properties, we integrated two previously validated LbL assembly strategies: (i) short-chain polycations alternated with HA to impart antibacterial activity,[29] and (ii) PLL_{30} alternated with Fn to limit bacterial adhesion and promote fibroblast attachment.[30] The central challenge was to determine whether these functional components could be combined within a single multilayer architecture without compromising their individual bioactivities, and to assess how the spatial positioning of Fn within the multilayer influences the physicochemical properties and biological performance.

Dip coating was selected as the fabrication method for architectural optimization due to its simplicity, reproducibility, and ability to provide precise control over LbL assembly.[24] This controlled deposition approach enables systematic investigation of architectural variables before transitioning to more complex deposition strategies. Here, glass substrates were used as a model substrate.

Two distinct architectural strategies for Fn incorporation were systematically investigated: (i) *Intercalated Fn architecture*, $[(PLL_{30}\text{-}HA)_2(PLL_{30}\text{-}Fn)]_4$, where Fn alternates with HA throughout the film thickness, resulting in Fn distribution across the entire multilayer; (ii) *Top-Layer Fn architecture*, $(PLL_{30}\text{-}HA)_6 + (PLL_{30}\text{-}Fn)_6$, where Fn is incorporated exclusively in the terminal layers onto a pre-assembled $(PLL_{30}\text{-}HA)_6$ base (Scheme 1A).

These two architectures were designed to probe the interplay between multilayer growth behaviour, Fn accessibility, and functional compartmentalization. The physicochemical characterization focused on monitoring the multilayer buildup, and growth profiles, providing insight into how architectural design governs the balance between antibacterial efficacy and cytocompatibility.

Multilayer assembly and film growth profile. Film assembly and growth characterization were performed *via* Attenuated Total Reflection-Fourier Transform Infrared (ATR-FTIR) spectroscopy and Quartz Microbalance with Dissipation monitoring (QCM-D), respectively.

ATR-FTIR spectroscopy was used to monitor the sequential adsorption process through characteristic amide I′ (ν(C═O), 1600–1700 cm^{-1}) and amide II′ (N–H bending, 1500–1600 cm^{-1}) bands (Fig. 1A and B). The progressive increases in amide I′ intensity at each deposition step confirmed multilayer buildup for both architectures, with Fn adsorption significantly higher compared to PLL_{30} or HA, reflecting its substantial incorporation.

To gain deeper insight into the film growth kinetics and mass deposition profiles, QCM-D experiments were performed. Due to instrumental thickness limitations, QCM-D monitoring

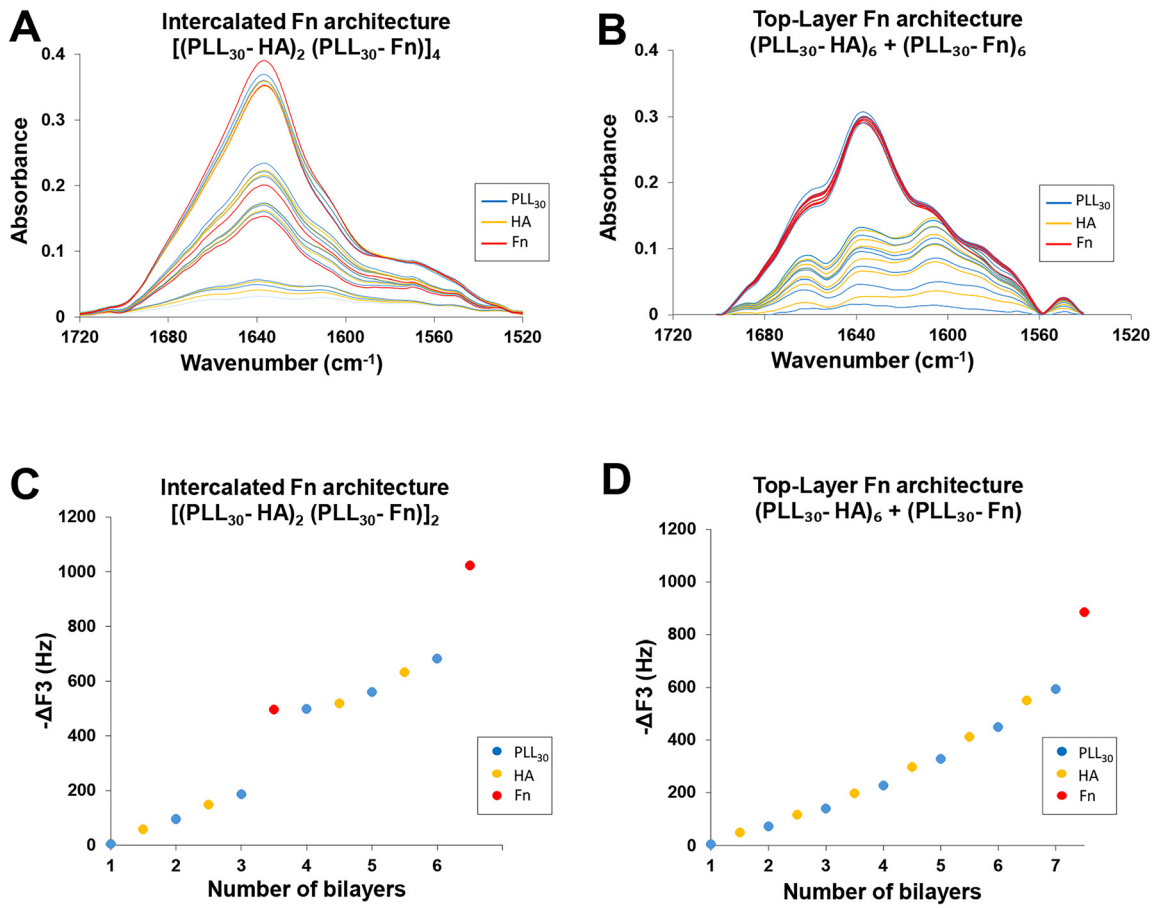

Fig. 1 Multilayer film assembly and growth profile. (A and B) LbL film assembly followed by ATR-FTIR. Spectra were acquired during the buildup of (A) Intercalated Fn architecture $[(PLL_{30}\text{-}HA)_2(PLL_{30}\text{-}Fn)]_4$ and (B) Top-Layer Fn architecture $(PLL_{30}\text{-}HA)_6 + (PLL_{30}\text{-}Fn)_6$ after each adsorption of PLL_{30} (blue), HA (orange) and Fn (red). Characteristic amide I′ band (1600–1700 cm^{-1}) confirm polyelectrolytes incorporation during LbL buildup. (C and D) Film buildup monitored by QCM-D on SiO_2-coated quartz crystals after each adsorption of PLL_{30} (blue), HA (orange) and Fn (red). Evolution of normalized frequency shift ($-\Delta f3$) at the third overtone (15 MHz) as a function of number of deposited layers for (C) Intercalated Fn architecture and (D) Top-Layer Fn architecture is shown.

was restricted to the first 6–7 bilayers. For both architectures an exponential growth kinetics was observed (Fig. 1C and D), with a pronounced frequency shift (ΔF) after the addition of Fn.

The exponential growth regime showed by QCM-D is consistent with the well-established behaviour of PLL/HA polyelectrolyte-based multilayers and reflects the high mobility of short-chain PLL_{30} within the film, enabling its "in-and-out" diffusion.[29,33] However, the two architectures differ structurally. The Intercalated Fn architecture sustained progressive amide I′ signal buildup up to 12 bilayers, while the Top-Layer configuration showed a lower amide I′ band signal progression following Fn deposition, in accordance with the sub-linear growth behaviour previously reported for Fn-terminated films.[30,32] These results may suggest that the Intercalated Fn architecture could result in a structurally thicker and more hydrated film compared to the Top-Layer Fn configuration, as reported in literature between linear and exponential growing multilayers.[33–35]

However, collectively, these physicochemical data demonstrate that PLL_{30}, HA, and Fn can be successfully co-assembled to form a multilayer using both intercalated and top-layer incorporation strategies.

Multilayer topography assessed by AFM. AFM analysis revealed distinct surface topographies across the two conditions (Fig. 2). The Intercalated Fn architecture (Fig. 2A and B) showed a heterogeneous surface with large, irregularly distributed globular aggregates (height scale ± 2 μm), throughout the multilayer. In contrast, the Top-Layer Fn architecture (Fig. 2C and D) exhibited a more homogeneous surface organization (height scale ± 1 μm) with smaller, more uniformly distributed features, that could be due to the terminal confinement of Fn at the outermost surface. The presence of aggregates is consistent with previous observations for $(PLL\text{-}Fn)_{10}$ coatings.[30]

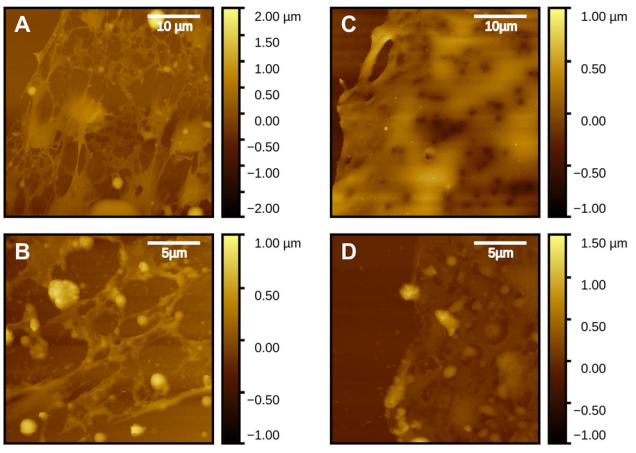

Fig. 2 Dip coating multilayer topography assessed by AFM. (A and B) Intercalated Fn architecture $[(PLL_{30}\text{-}HA)_2(PLL_{30}\text{-}Fn)]_4$. (C and D) Top-Layer Fn architecture $(PLL_{30}\text{-}HA)_6 + (PLL_{30}\text{-}Fn)_6$. 12 mm diameter round glass slides were used as substrate.

The mean surface roughness (Sa) of the coating architectures, by independently analyzing bare glass scratch areas, lower coating regions, and aggregate features are presented in SI Table S1. Glass scratch areas showed consistent Sa values of 10–30 nm across the two conditions. The Intercalated Fn architecture exhibited a greater heterogeneity, with fibrillar structures at Sa of 40 to 150 nm and aggregates reaching 150 to 400 nm, while the Top-Layer Fn architecture showed a more uniform profile with lower regions at Sa of 30 to 80 nm and aggregates of 150 to 250 nm, reflecting a less heterogeneous Fn surface distribution within the coating.

Multilayer films cytocompatibility with human gingival fibroblasts. The spatial distribution of Fn within the films could significantly affect their compatibility with eukaryotic cells. Here, the cytocompatibility of the $(PLL_{30}\text{-}HA)_6$ film, the Top-Layer Fn architecture and the Intercalated Fn architecture was evaluated using human gingival fibroblasts (HGF), the primary cells involved in soft tissue sealing around dental implants. After 24 h of direct contact, significant differences in cell compatibility were observed depending on Fn positioning (Fig. 3A).

The $(PLL_{30}\text{-}HA)_6$ coating demonstrated acceptable biocompatibility with HGF, achieving 72% metabolic activity relative to uncoated glass controls. However, the addition of $(PLL_{30}\text{-}Fn)_6$ terminal layers in the Top-Layer Fn architecture significantly enhanced cytocompatibility to 78% ($p < 0.05$ *vs.* $(PLL_{30}\text{-}HA)_6$). Conversely, the Intercalated Fn architecture $[(PLL_{30}\text{-}HA)_2(PLL_{30}\text{-}Fn)]_4$ exhibited significantly reduced metabolic activity (54%, $p < 0.05$ *vs.* Top-Layer Fn architecture).

Cell morphology was investigated by vinculin immunostaining and it revealed a clear Fn dependent effect on cell morphology and focal adhesion formation (Fig. 3B). Cells on $(PLL_{30}\text{-}HA)_6$ without Fn displayed a round-shaped morphology with minimal actin organization and no remarkable focal adhesion. In contrast, both Fn-containing architectures supported cell spreading with the typical elongated morphology, abundant actin cytoskeleton and focal adhesion assembly. Particularly, a higher vinculin lamellipodia formation, very similar as the glass control, is visible in the Top-Layer Fn configuration, rather than in the Intercalated Fn architecture, supporting HGF adhesion on the coatings. The impact of Fn on cell's focal adhesion was already observed on the pro-adhesive $(PLL_{30}\text{-}Fn)_{10}$ films,[30] in which vinculin appears distributed not only in the cytoplasm but also at the cell periphery. Here, vinculin spreads in the same way in the Top-Layer Fn architecture.

This suggests that the surface-exposed Fn is necessary for a positive fibroblast response. To investigate this hypothesis, the surface accessible Fn and cell binding domain (CBD) sites were analysed by ELISA assay.

ELISA quantification of surface-accessible Fn and its CBD confirmed for both architectures a significantly higher Fn and CBD content compared to a Fn-only adsorbed monolayer (OD_{450} = 2.78 ± 0.09 and 2.36 ± 0.07 *vs.* 1.63 ± 0.03 for Fn; 0.4 ± 0.04 and 0.36 ± 0.04 *vs.* 0.26 ± 0.04 for CBD, for Top-Layer Fn, Intercalated Fn, and Fn monolayer respectively; mean ± SD).

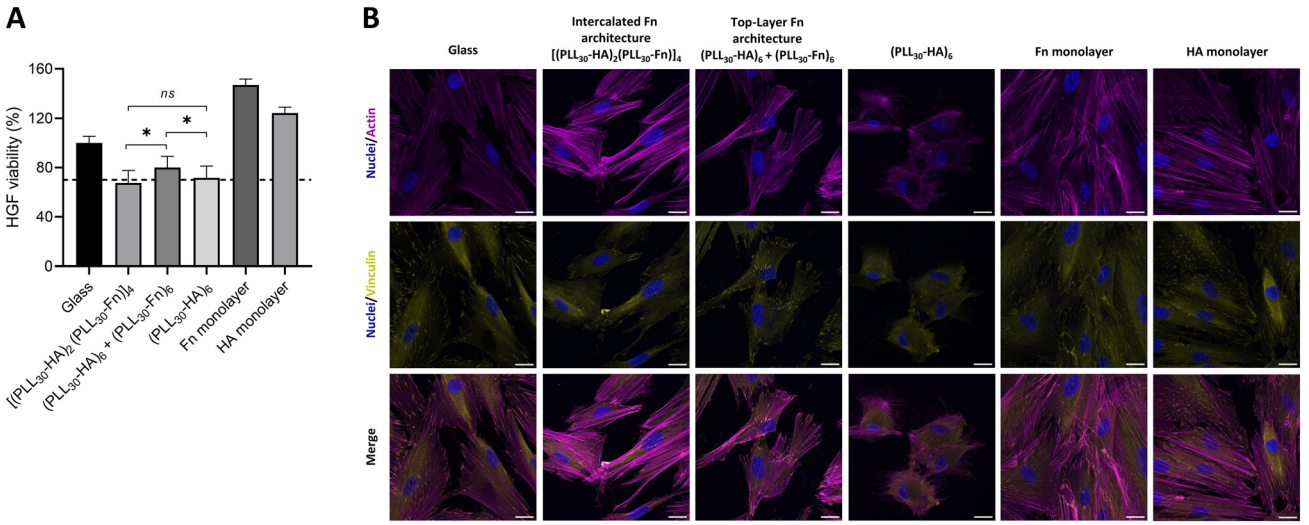

Fig. 3 (A) Metabolic activity of HGF after 24 h of direct contact with dip-coated multilayer films on glass substrates. Results are expressed as percentage of uncoated glass control (100% viability). (*$p < 0.05$, one-way ANOVA). Error bars represent standard deviation. Dashed line indicates 70% metabolic activity threshold. (B) Representative morphology and focal adhesion of human gingival fibroblasts (HGF) after 24 h of incubation on different multilayer films immunolabelled with antivinculin (focal adhesion, yellow), and stained with DAPI (nuclei, blue) and phalloidin (actin, magenta). A higher distribution of vinculin lamellipodia on the Top-Layer Fn architecture is visible. Scale bar 20 μm. Glass slides of 12 mm diameter were used as substrate.

This confirms that multilayer assembly significantly enriches the surface with Fn and CBD sites.

Interestingly, while the CBD accessibility was comparable between the two LbL architectures (OD_{450} = 0.4 *vs.* 0.36), the Fn content was higher in the Top-Layer Fn architecture. These observations suggest that differences in cytocompatibility are governed by the entire coating organisation. The thicker and more hydrated profile of the Intercalated Fn architecture results in an excessively soft substrate for optimal cell response, which has been shown to impair fibroblast anchoring, spreading, and proliferation on PLL/HA-based multilayers.[36,37] Indeed the modest response of $(PLL_{30}\text{-}HA)_6$ alone (72%) is consistent with this interpretation, while the addition of Fn in outermost layers enables focal adhesion. Moreover, AFM analysis demonstrated that the Top-Layer Fn architecture displayed a more homogeneously distributed coating, whereas the Intercalated Fn configuration exhibited large aggregates and more heterogeneous topography. The more homogeneous surface organization of the Top-Layer Fn architecture, together with the higher total surface accessible Fn, facilitate cell adhesion and the subsequent well-known cell-mediated matrix remodelling, thereby contributing to the improved cytocompatibility observed for the Top-Layer Fn configuration.

Antibacterial properties of the multilayer coatings: early bacterial adhesion and biofilm prevention under oral-mimicking conditions. The early antibacterial adhesion efficacy of both architectural designs was assessed against two clinically relevant bacterial pathogens: *S. aureus* (Gram-positive) and *A. actinomycetemcomitans* (Gram-negative), both associated with *peri*-implant infection.[14–18]

Following a 2-hour exposure to bacterial suspensions (10^6 CFU mL^{-1} in PBS), on glass substrate as reference $(3.50 \pm 0.54) \times 10^3$ CFU cm^{-2} and $(6.31 \pm 4.09) \times 10^3$ CFU cm^{-2} were detected for *S. aureus* and *A. actinomycetemcomitans*, respectively. In contrast, both the Intercalated Fn and Top-Layer Fn architectures achieved 100% inhibition of bacterial adhesion for both pathogens, with no detectable adherent bacteria on coated surfaces. This early-stage anti-adhesive property suggests that the incorporation of Fn into PLL_{30}/HA coatings does not compromise the antibacterial properties conferred by the cationic PLL_{30}. Moreover, the complete inhibition observed against both Gram-positive and Gram-negative bacteria reflects a broad-spectrum, membrane-disruption mechanism rather than species-specific binding, driven by direct polycation contact with bacterial membrane.[29] Furthermore, the antibacterial efficacy was independent of Fn positioning and both architectures achieved complete bacterial inhibition, indicating that sufficient polycationic charge remains accessible at the coating surface in both configurations to interact with and inactivate bacteria upon initial contact.

To validate if the films are compatible with biomedical applications, the cytocompatible Top-Layer Fn architecture $(PLL_{30}\text{-}HA)_6$ + $(PLL_{30}\text{-}Fn)_6$ was deposited by dip-coating onto medical-grade titanium substrates used in clinic (Ti6Al4V-ELI) and challenged with *S. aureus* in diluted culture medium (10% TSB in PBS) to simulate the limited nutrient availability in *in vivo* conditions. Bacterial adhesion and biofilm formation were assessed at 8 h and 24 h (Fig. 4). Uncoated titanium substrates exhibited a substantial bacterial colonization that progressed from $(5.76 \pm 2.86) \times 10^3$ CFU cm^{-2} after 8 h to $(4.79 \pm 0.11) \times 10^4$ CFU cm^{-2} after 24 h. In contrast, coated titanium

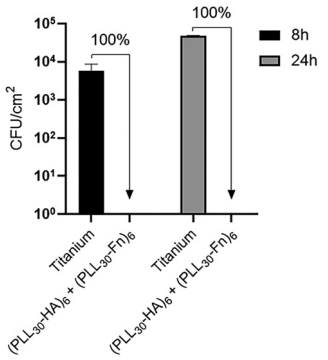

Fig. 4 Anti-adhesive and antibiofilm properties of dip-coating Top-Layer Fn architecture on titanium surface under oral-mimicking conditions. Biofilm formation was quantified by CFU counting after 8 h and 24 h in contact with *S. aureus* in diluted medium (10% TSB in PBS) on uncoated and dip-coated titanium (9 mm diameter). Complete inhibition of bacterial adhesion and biofilm formation was observed. Error bars represent standard deviation.

achieved complete inhibition of bacterial adhesion and biofilm formation at both timepoints.

The fact that the Top-Layer Fn architecture maintains a robust antibacterial activity independently of the underlying substrate suggests that the antibacterial mechanism relies on the coating's polycation accessibility rather than substrate-dependent polyelectrolyte adsorption behaviour, with the polycation remaining available at the coating surface for up to 24 h under oral-mimicking conditions.

These findings reveal a critical functional asymmetry between the two architectures: while both Intercalated Fn and Top-Layer Fn architectures provide an equivalent anti-adhesive protection against bacteria, only the Top-Layer Fn configuration successfully balances it with cytocompatibility. This divergence reflects the distinct molecular requirements for bacterial inhibition and cell adhesion. Cell adhesion requires spatially accessible Fn at the film surface, while antibacterial activity relies on PLL_{30} "in and out" diffusion within the film to disrupt bacterial membranes,[29] regardless of Fn positioning. This functional asymmetry guided the selection of the Top-Layer Fn architecture $(PLL_{30}\text{-}HA)_6 + (PLL_{30}\text{-}Fn)_6$ for spray-coating development.

Transition to spray-assisted deposition

While dip-coating offers a robust and well-controlled platform for the systematic engineering of bifunctional PLL_{30}/HA/Fn LbL interfaces, its use for practical dental applications is limited. Specifically, the prolonged assembly times and the immersion of implants in multiple solutions, characteristic of the dip-coating process, are incompatible with *in situ* or chairside clinical use. For this reason we explored alternative deposition strategies for a rapid, chairside-applicable coating technique that could transform the management of *peri*-implantitis, using a portable dual-syringe spray device developed by SPARTHA Medical (Scheme 1B). This system allows the simultaneous nebulization of polycation and polyanion solutions from independent reservoirs, thereby eliminating intermediate rinsing steps and reducing total coating time to less than 1 minute. The spray-assisted deposition could indeed be used for the prevention of *peri*-implantitis by depositing the coating prior to surgical placement to provide antibacterial protection during the vulnerable early healing phase or as a curative *in situ* treatment of *peri*-implantitis on already-placed implants, where coating deposition must occur directly in the oral cavity without the removal of the device. The importance of the transition from dip-coating to an *in situ* spray-applicable coating rely on the possibility of the reapplication of the coating in clinical setting to overcome several issues such as (i) the eventual erosion of the coating onto the pre-coated implant caused by mechanical stresses during its placement, or (ii) the coating degradation over time.

However, transitioning from dip-coating to spray-coating proved challenging. Spray deposition operates under fundamentally different kinetic conditions, such as the polyelectrolytes adsorption that occurs during brief contact, and rapid evaporation at the substrate interface.[38,39] The film formation is more likely governed by the concentrations and charge ratio of the components.[40] Indeed, initial experiments using the polyelectrolyte and Fn concentrations optimized for dip-coating (0.5 mg mL^{-1}) produced highly variable antibacterial performance. Bacterial inhibition on titanium surfaces coated *via* the same spray process ranged from 20% to 99%, indicating insufficient polycation deposition across the samples. Systematic concentration optimization achieved reproducible film formation with consistent antibacterial activity: PLL_{30} 10 mg mL^{-1} (20-fold increase *vs.* dip-coating); HA 5 mg mL^{-1} (10-fold increase) and Fn 1.0 mg mL^{-1} (2-fold increase). These concentrations are coherent to a previous study using the same dual-syringe spray system, that identified the optimal formulation for reproducible antimicrobial coating against *S. aureus* and *Pseudomonas aeruginosa*.[41]

Visualization of spray-coated films on titanium surfaces. The simultaneous nebulization of both polyelectrolyte solutions of the spray-coating deposition precludes the step-by-step monitoring of film assembly accessible during dip-coating *via* QCM-D and ATR-FTIR. To confirm the successful deposition of the bifunctional coating and the distribution of its components, the spray-assisted multilayer film was visualized using confocal laser scanning microscopy (Carl Zeiss) with fluorescently labeled PLL_{30}-FITC (cyan) and Fn-Alexa568 (red). Confocal images confirmed the successful deposition of the coating on titanium surfaces, with homogeneous coverage across the entire substrate (Fig. 5). The distribution of Fn showed co-localization with PLL_{30}, but appeared as discrete aggregates rather than a continuous layer. This Fn aggregation behaviour is consistent with previous observations in dip-coating LbL-assembled Fn films.[30,32]

Notably, the underlying titanium topography, characterized by surface striations did not influence the organization of the coating. A homogeneous distribution of PLL_{30} and Fn was observed across the entire surface, without alignment along the underlying striation patterns indicating that this coating

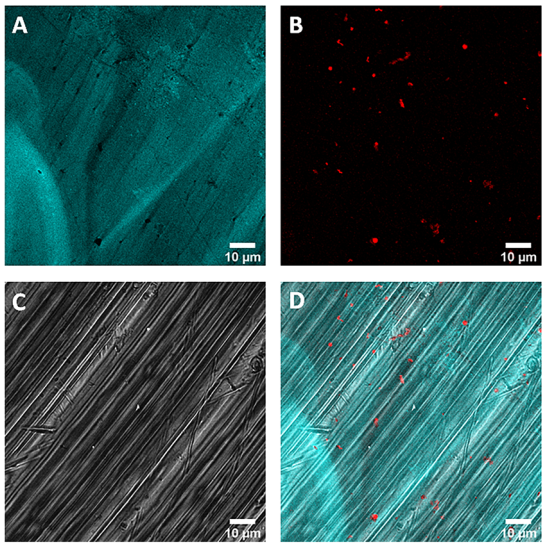

Fig. 5 Confocal laser scanning microscopy images of spray-coated (PLL_{30}-HA) + (PLL_{30}-Fn) 0.5 mg mL^{-1} films on titanium substrates. (A) PLL_{30} channel (cyan), (B) Fn channel (red), (C) titanium substrate topography, and (D) merged image showing co-localization of PLL_{30} and Fn. Scale bar: 10 µm. Ti disks of 9 mm diameter were used as substrate.

could be applied uniformly regardless of the underlying substrate.

Film thickness could not be quantified by confocal microscopy, as the coatings were below the resolution limit for *z*-stack analysis. This is consistent with the observation that spray-coated films are thinner than dip-coated films.[38]

Multilayer topography assessed by AFM. AFM analysis of spray-deposited SPR (PLL_{30}-HA) 2.5 mL + (PLL_{30}-Fn) 1.25 mL coatings on glass substrates also confirmed successful film formation, with surface features and aggregates comparable to the dip-coated Top-Layer Fn architecture (Fig. 6). Immersion of the spray coatings in PBS for 7 days confirmed structural integrity of the film, with no evidence of delamination or loss of surface morphology compared to

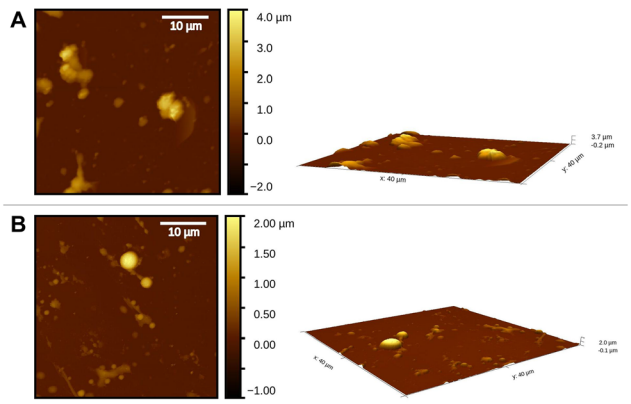

Fig. 6 2D and 3D AFM topography of spray-coated (PLL_{30}-HA) + (PLL_{30}-Fn) films. Scale bar: 10 µm. Round glass slides of 12 mm diameter were used as substrate.

the same coating at day 1, providing preliminary evidence of coating stability under physiological conditions (data not shown). These results are consistent with recent studies by FIB-SEM cross-sectional analysis of the film thickness and characterisation of spray-deposited PAR_{30}/HA polyelectrolyte coatings on medical-grade titanium using the same dual-syringe spray device.[41] Although the polycationic component differs between that study (PAR_{30}) and the present work (PLL_{30}), both systems rely on the same electrostatic LbL assembly mechanism, the same dual-syringe spray device, and the same HA polyanion, supporting the relevance of these thickness measurements on Ti substrates. Spray-deposited coatings exhibited a consistent mean roughness (Sa) of glass Sa = 10–20 nm, lower coated regions of Sa = 150–200 nm, and a higher Sa of aggregates of 550–650 nm (SI Table S1), that reflects the rapid complexation kinetics of spray-assisted deposition compared to the dip coating architectures.

Cytocompatibility of spray-coated titanium. Cell compatibility was evaluated using Balb/3T3 fibroblasts, a standardized cell line commonly employed for biocompatibility testing, selected for spray-coating validation due to their robustness and standardized response, facilitating protocol optimization.

During spray-coating optimization, we found that polyelectrolyte counterion chemistry significantly impacts cytocompatibility in spray-deposited films, but not in dip-coated ones. $PLLKB_{30}$ produced cytotoxic surfaces under spray conditions, whereas $PLLKC_{30}$ yielded cytocompatible coatings (SI Fig. S1). This difference likely arises from the absence of rinsing steps in spray deposition, leading to retention of counterions – such as bromide – that may contribute to cytotoxicity. Consequently, all subsequent spray-coating experiments were performed using $PLLKC_{30}$.

Early fibroblast responses were evaluated through an initial cytocompatibility screening on spray-coated glass coverslips using a 4-hour adhesion assay. The spray-coated samples supported cell viability and displayed higher metabolic activity when terminal Fn was incorporated (SPR (PLL_{30}-HA) + (PLL_{30}-Fn)), achieving 85%, compared to coatings without the terminal PLL_{30}/Fn (63% for SPR (PLL_{30}-HA), $p < 0.05$) (Fig. 7A). This response profile mirrors the cellular response observed for dip-coated film, where the incorporation of terminal PLL_{30}/Fn layers similarly enhances cell adhesion compared to PLL_{30}/HA-only coatings. This parallel suggests that the spray-assembled PLL_{30}/HA films retain the characteristic of hydrated coating as seen for dip-coatings, and that the surface-exposed Fn compensates this hydration by providing accessible integrin-binding sites for cell attachment.

These results confirmed that the spray-coating process itself employing concentrations of PLL_{30} (10 mg mL^{-1}), HA (5 mg mL^{-1}), and Fn (1 mg mL^{-1}) without intermediate rinsing, can produce cytocompatible coatings.

Thus, cell viability was assessed by seeding fibroblasts on both spray-coated and uncoated titanium substrates, cultured for 24 h. To mimic the *peri*-implant environment, in which implants come into contact with blood serum and gingival

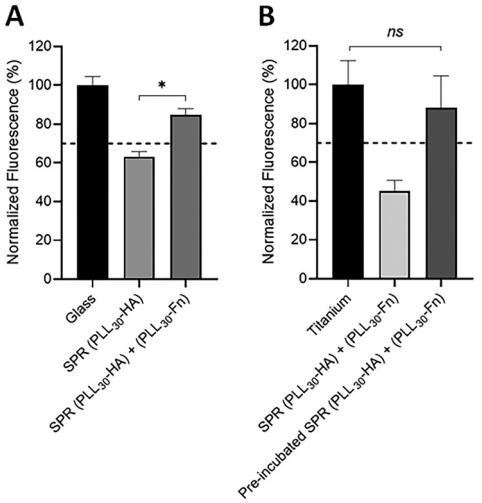

Fig. 7 Cytocompatibility of spray-coated glass and titanium substrates. (A) Fibroblast early response after 4 h of direct contact on spray-coated glass substrates with or without terminal PLL_{30}/Fn. Fn-containing films showed higher response compared to Fn-free coatings. (B) Fibroblasts metabolic activity after 24 h of direct contact with spray-coated titanium substrates with or without FBS pre-incubation. Results are normalized to uncoated control (100%) (*$p < 0.05$, one-way ANOVA). Error bars represent standard deviation. Dashed line indicates 70% metabolic activity threshold. Round glass slides of 12 mm diameter and Ti discs of 9 mm diameter were used as substrate.

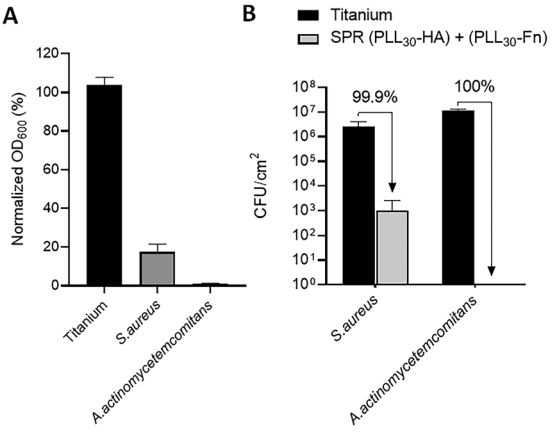

Fig. 8 Antibacterial properties of spray-coated titanium. (A) Bacterial growth in planktonic phase after 24 h contact of spray-coated titanium substrates with *S. aureus* and *A. actinomycetemcomitans* normalized to uncoated titanium controls (100% growth). (B) *S. aureus* and *A. actinomycetemcomitans* biofilm formation on uncoated titanium and spray-coated titanium substrates quantified by CFUs counting. Error bars represent standard deviation. Ti discs of 9 mm diameter were used as substrate.

fluids rich in proteins that spontaneously adsorb onto implant surfaces, coated substrates were pre-incubated with fetal bovine serum (1 h at 37 °C) prior to cell seeding. This pre-conditioning significantly enhanced cell viability. Under these optimized conditions, spray-coated titanium substrates increased cell viability from 45% to 88% after 24 h culture (Fig. 7B), substantially approaching the viability of uncoated titanium controls.

Antibacterial properties of spray-coated titanium. Spray-coated titanium substrates were challenged with *S. aureus* and *A. actinomycetemcomitans* for 24 h. Both planktonic bacterial growth in the surrounding medium and surface-associated biofilm formation were assessed.

Spray-coated surfaces significantly reduced planktonic bacterial growth compared with uncoated titanium controls, as evidenced by the lower optical density values (OD_{600}) in the surrounding medium (Fig. 8A).

Moreover, spray-coated substrates exhibited strong inhibition of surface-associated biofilm formation for both pathogens. A significant reduction in biofilm formation was observed against *S. aureus*, while a complete inhibition was achieved against *A. actinomycetemcomitans* (Fig. 8B).

Overall, the concomitant inhibition of planktonic growth and surface biofilm formation demonstrates that the translation to a clinically compatible spray-assisted deposition preserves the polycation mobility at concentrations sufficient to achieve a robust antibacterial performance by contact-killing, although the construction method differs substantially from that of the dip-coating.

Conclusions

In this study, we demonstrate that bifunctional multilayer coatings combining antibacterial and cytocompatible functionalities can be rationally designed through architectural control and successfully translated from dip-coating technique to a rapid, clinically applicable spray-coating deposition. By combining short-chain polycations (PLL_{30}), hyaluronic acid (HA), and fibronectin (Fn) within the Layer-by-Layer assembly (Scheme 1A), we established that Fn spatial localization is crucial for dual functionality: confining Fn to terminal layers – Top-Layer Fn architecture $(PLL_{30}\text{-}HA)_6 + (PLL_{30}\text{-}Fn)_6$ – preserves both antibacterial activity and cytocompatibility, whereas distributing Fn throughout the film compromises cell adhesion despite equivalent inhibition of bacterial adhesion.

The central achievement of this work is the successful translation of this dip-coated architecture to an innovative spray-assisted deposition using a dual-syringe spray device developed by SPARTHA Medical (Scheme 1B), reducing coating assembly time from several hours to less than 1 minute. The translation required comprehensive re-optimization but enabled preservation of bifunctional performance on medical-grade titanium substrates.

The clinical impact of spray-assisted rapid deposition is substantial. It can be applied in two scenarios: preventive coating of sterile implants immediately before surgical placement, and potential curative *in situ* application during *peri*-implantitis treatment, without device removal, thereby transforming a laboratory concept into a practical, chairside-applicable platform for both preventive and curative management of *peri*-implantitis. Building on this translational foundation, future investigations will assess the spray-coated bifunctional system in advanced 3D and co-culture models before progres-

sing toward *in vivo* evaluations, in parallel with miniaturization of the deposition device for full chairside integration.

Author contributions

AG, EP, NEV and PL contributed to the conception and supervision of the study. DS contributed to the design of antimicrobial activity. RC contributed to the development of cell gingival response. GS, DS, RC, LM, YL, CC, RA and GF contributed to the experiments. NC contributed to the Titanium supply and characterization. GS performed the statistical analysis. GS and AG wrote the first draft of the manuscript. All authors contributed to the manuscript revision and read and approved the submitted version.

Conflicts of interest

There are no conflicts to declare.

Data availability

Data for this article, including raw experimental data, antibacterial assay results, and dip coating characterization (ATR-FTIR, QCM-D), are available in Zenodo at https://doi.org/10.5281/zenodo.18788944.

Supplementary information (SI) is available. See DOI: https://doi.org/10.1039/d6bm00291a.

Acknowledgements

Authors would like to acknowledge the funding from the French National Research Agency (ANR) through the BioImTiTis ANR project and to thank Anne-Lise Chopard-Lallier from one of the consortium members, Anthogyr, for the provision and preparation of the titanium substrates used in this study. The authors are grateful to Caroline Gorin (UMR1333 Oral Health, Université Paris Cité, France) for the isolation and kind donation of primary human gingival fibroblasts (HGF). The authors also thank Bernard Senger (INSERM, Strasbourg, France) for his contribution to the QCM-D characterization of dip-coated films and for his assistance in the analysis of QCM-D data. Authors thank the imaging facility "Microscopies & Analyses" (Federation I-Mat, CY Cergy-Paris University), where confocal microscopy was carried out. Authors further thank Valentina Sorvillo (Vanvitelli University, Naples, Italy) for her assistance in preparing the schematic illustrations of this article.

References

1 H. W. Elani, J. R. Starr, J. D. Da Silva and G. O. Gallucci, *J. Dent. Res.*, 2018, **97**, 1424–1430.
2 M. E. Galarraga-Vinueza, S. Pagni, M. Finkelman, T. Schoenbaum and L. Chambrone, *J. Periodontol.*, 2025, **96**, 587–633.
3 D. R. Dixon and R. M. London, *Periodontology 2000*, 2019, **81**, 167–178.
4 B. Klinge, A. Klinge, K. Bertl and A. Stavropoulos, *Eur. J. Oral Sci.*, 2018, **126**, 88–94.
5 R. M. Donlan and J. W. Costerton, *Clin. Microbiol. Rev.*, 2002, **15**, 167–193.
6 P. Diaz, E. Gonzalo, L. J. G. Villagra, B. Miegimolle and M. J. Suarez, *BMC Oral Health*, 2022, **22**, 449.
7 J. Derks and C. Tomasi, *J. Clin. Periodontol.*, 2015, **42**, S158–S171.
8 D. Herrera, T. Berglundh, F. Schwarz, I. Chapple, S. Jepsen, A. Sculean, M. Kebschull, P. N. Papapanou, M. S. Tonetti, M. Sanz and EFP workshop participants and methodological consultant, *J. Clin. Periodontol.*, 2023, **50**, 4–76.
9 M. Abdallah, Z. Badran, O. Ciobanu, N. Hamdan and F. Tamimi, *Adv. Healthcare Mater.*, 2017, **6**, 1700549.
10 A. G. Gristina, *Science*, 1987, **237**, 1588–1595.
11 H. J. Busscher, H. C. Van Der Mei, G. Subbiahdoss, P. C. Jutte, J. J. A. M. Van Den Dungen, S. A. J. Zaat, M. J. Schultz and D. W. Grainger, *Sci. Transl. Med.*, 2012, **4**, 153rv10.
12 G. R. Persson and S. Renvert, *Clin. Implant Dent. Relat. Res.*, 2014, **16**, 783–793.
13 L. Hall-Stoodley, J. W. Costerton and P. Stoodley, *Nat. Rev. Microbiol.*, 2004, **2**, 95–108.
14 S. Renvert, C. Lindahl, H. Renvert and G. R. Persson, *Clin. Oral Implants Res.*, 2008, **19**, 342–347.
15 P. Sahrmann, F. Gilli, D. B. Wiedemeier, T. Attin, P. R. Schmidlin and L. Karygianni, *Microorganisms*, 2020, **8**, 661.
16 L. G. Harris and R. G. Richards, *J. Mater. Sci.: Mater. Med.*, 2004, **15**, 311–314.
17 T. Thurnheer and G. N. Belibasakis, *Clin. Oral Implants Res.*, 2016, **27**, 890–895.
18 W. F. Oliveira, P. M. S. Silva, R. C. S. Silva, G. M. M. Silva, G. Machado, L. C. B. B. Coelho and M. T. S. Correia, *J. Hosp. Infect.*, 2018, **98**, 111–117.
19 M. Croes, S. Bakhshandeh, I. A. J. van Hengel, K. Lietaert, K. P. M. van Kessel, B. Pouran, B. C. H. van der Wal, H. C. Vogely, W. V. Hecke, A. C. Fluit, C. H. E. Boel, J. Alblas, A. A. Zadpoor, H. Weinans and S. A. Yavari, *Acta Biomater.*, 2018, **81**, 315–327.
20 T. D. Michl, B. R. Coad, M. Doran, M. Osiecki, M. H. Kafshgari, N. H. Voelcker, A. Hüsler, K. Vasilev and H. J. Griesser, *Chem. Commun.*, 2015, **51**, 7058–7060.
21 S. L. Bellis, *Biomaterials*, 2011, **32**, 4205–4210.
22 A. Oyane, K. Hyodo, M. Uchida, Y. Sogo and A. Ito, *J. Biomed. Mater. Res.*, 2011, **97B**, 96–104.
23 S. Ghadhab, I. Bilem, A. Guay-Bégin, P. Chevallier, F. A. Auger, J. Ruel, E. Pauthe and G. Laroche, *J. Biomed. Mater. Res.*, 2021, **109**, 2187–2198.
24 G. Decher, J. D. Hong and J. Schmitt, *Thin Solid Films*, 1992, **210–211**, 831–835.

25 Q. Shi, Z. Qian, D. Liu and H. Liu, *Front. Physiol.*, 2017, **8**, 574.
26 H. Hartmann and R. Krastev, *BioNanoMaterials*, 2017, **18**, 20160015.
27 O. A. Ouni, G. Subbiahdoss, A. Scheberl and E. Reimhult, *Materials*, 2021, **14**, 4596.
28 Z. Zhang, J. Zeng, J. Groll and M. Matsusaki, *Biomater. Sci.*, 2022, **10**, 4077–4094.
29 A. Mutschler, L. Tallet, M. Rabineau, C. Dollinger, M.-H. Metz-Boutigue, F. Schneider, B. Senger, N. E. Vrana, P. Schaaf and P. Lavalle, *Chem. Mater.*, 2016, **28**, 8700–8709.
30 A. Miranda, D. Seyer, C. Palomino-Durand, H. Morakchi-Goudjil, M. Massonie, R. Agniel, H. Rammal, E. Pauthe and A. Gand, *Front. Bioeng. Biotechnol.*, 2022, **9**, 807697.
31 L. Poulouin, O. Gallet, M. Rouahi and J.-M. Imhoff, *Protein Expression Purif.*, 1999, **17**, 146–152.
32 A. Gand, M. Tabuteau, C. Chat, G. Ladam, H. Atmani, P. R. V. Tassel and E. Pauthe, *Colloids Surf., B*, 2017, **156**, 313–319.
33 C. Picart, J. Mutterer, L. Richert, Y. Luo, G. D. Prestwich, P. Schaaf, J.-C. Voegel and P. Lavalle, *Proc. Natl. Acad. Sci. U. S. A.*, 2002, **99**, 12531–12535.
34 Ph. Lavalle, C. Gergely, F. J. G. Cuisinier, G. Decher, P. Schaaf, J. C. Voegel and C. Picart, *Macromolecules*, 2002, **35**, 4458–4465.
35 C. Picart, Ph. Lavalle, P. Hubert, F. J. G. Cuisinier, G. Decher, P. Schaaf and J.-C. Voegel, *Langmuir*, 2001, **17**, 7414–7424.
36 N. Madaboosi, K. Uhlig, S. Schmidt, A. S. Vikulina, H. Möhwald, C. Duschl and D. Volodkin, *Macromol. Biosci.*, 2018, **18**, 1700319.
37 L. Richert, F. Boulmedais, P. Lavalle, J. Mutterer, E. Ferreux, G. Decher, P. Schaaf, J.-C. Voegel and C. Picart, *Biomacromolecules*, 2004, **5**, 284–294.
38 A. Izquierdo, S. S. Ono, J.-C. Voegel, P. Schaaf and G. Decher, *Langmuir*, 2005, **21**, 7558–7567.
39 P. Schaaf, J. Voegel, L. Jierry and F. Boulmedais, *Adv. Mater.*, 2012, **24**, 1001–1016.
40 M. Lefort, F. Boulmedais, L. Jierry, E. Gonthier, J. C. Voegel, J. Hemmerlé, Ph. Lavalle, A. Ponche and P. Schaaf, *Langmuir*, 2011, **27**, 4653–4660.
41 Y. Li, S. Hathroubi, O. Heck, L. Lieu, L. Petit, X. Wurtz, A. Rekiki, A. Gaudin, N. Canourgues, D. Mercer, M. Tunali, B. Nowack, P. Meier, G. Reina, P. Wick, M. Safarzadeh, A. Demircan, D. Grossin, C. Drouet, T. Soubrié, T. Holdanova, M. Kremer, N. Willem, S. Jester, A. Cès, C. Calligaro, B. Letellier, A. Dupret-Bories, P. Lavalle and N. Vrana Engin, *bioRxiv*, 2026, DOI: 10.64898/2026.04.10.717441.

